THE JOURNAL OF PHYSICAL CHEMISTRY Letters

Viewpoint

Cite This: J. Phys. Chem. Lett. 2019, 10, 2767−2774

pubs.acs.org/JPCL

Fundamental Studies of Relationships between Experimental Nonlinear Coherent Vibrational Spectroscopies

This contribution examines the creation of vibrational coherences and the output signal and shows that the efficiency of two-dimensional infrared (2D-IR) excitations is limited when the excitation pulses are much shorter than the coherence dephasing times. It does not treat nonlinear electronic spectroscopies where the dephasing times are much faster than typical excitation pulse widths so the electronic coherence amplitudes already reach the steady state. Using a simple closed form solution of the Liouville equation, this Viewpoint derives the coherence and output signal amplitudes using realistic conditions for different nonlinear vibrational methods.[1] The results allow direct comparisons between 2D-IR spectroscopy,[2−4] stimulated photon echo (SPE),[5] pump−probe,[6] transient absorption (TA),[7] transient grating (TG), triply vibrationally enhanced spectroscopy (TRIVE),[8] doubly vibrationally enhanced (DOVE) spectroscopy,[9−11] triply resonant sum frequency (TRSF) spectroscopy,[12−14] coherent anti-Stokes Raman spectroscopy (CARS),[15] stimulated Raman spectroscopy (SRS),[16] and femtosecond SRS (FSRS),[17] and the experimental compromises that control the capabilities and limitations of these methods. In particular, this Viewpoint focuses on understanding the factors that control how these methodologies can be used for measuring the wide range of modes that are important in vibrational spectroscopy. This Viewpoint (1) identifies why 2D-IR is constrained to the strongest vibrational transitions while FSRS covers the entire vibrational region, (2) estimates the relative signal levels for fully coherent and partially coherent 2D-IR, (3) compares nonlinear infrared spectroscopies with those involving Raman transitions, (4) identifies the importance of the duty cycle and nonresonant background in determining detection limits, (5) compares heterodyne and homodyne detection, and (6) discusses the extension of nonlinear methodologies to single-molecule vibrational spectroscopy. Identifying the factors that control these measurements can provide guidelines for designing experiments and developing experimental systems that optimize vibrational spectroscopy applications.

Theory. Nonlinear vibrational spectroscopies are based on creating coherences that form a Schrödinger cat superposition state where the photon fields and molecular quantum states exist in multiple states simultaneously. Although CMDS is not usually described using cat states, the cat state description is particularly important in recognizing the fundamental properties of CMDS. The cat state character of CMDS coherences makes it clear that the quantum states of a molecule and the excitation and output photon fields are entangled. A measurement of a molecular state or a photon field collapses the cat state and defines the states of the remaining molecular and photon fields. Measurements can be made by identifying the state resulting from the collapse of the cat state, the increase or decrease in the excitation field intensities, or the presence of a new photon field created by the output coherence. Examples of the different measurement strategies are 2D-IR and stimulated photon echo, inverse Raman and stimulated Raman, or CARS and TRSF, respectively. They are all different aspects of the same four-wave mixing process. Moreover, the nature of the CMDS cat state makes it clear why the measurement of a coherence is a fingerprint of the states and the direct coupling between the states of the original superposition state. It also makes it clear why the spectral fingerprint is immune to population relaxation effects because any population relaxation destroys the cat state.

A cat state wave function is given by $\Psi(x, t) = \sum_{\substack{m=\text{all vibr, elect,}\\ \text{photonic states}}} c_m(t)\psi_m(x)e^{i(\vec{k}_m\cdot\vec{z}-\omega_m t)}$. Dirac bra-ket notation describes the amplitude and the temporal and spatial phase relationships between pairs of states in the cat state, $\rho_{mn} \equiv c_m c_n^* = \tilde{\rho}_{mn} e^{i[\vec{k}_{mn}\cdot\vec{z}-(\omega_{mn}-i\Gamma_{mn})t]}$ where $\tilde{\rho}_{mn}$, $\vec{k}_{mn}\cdot\vec{z}$, ω_{mn}, and Γ_{mn} are the amplitude, spatial phase factor, frequency, and dephasing rate of the mn coherence, respectively. The spatial phase factors define the phase-matching conditions between the nonlinear polarization and the field it creates. The Liouville equation in the Bloch formalism describes how an electromagnetic wave drives the ket or bra transitions of an initial coherence into a different coherence.

$$\dot{\rho}_{ij} = -i\delta_{ij}\rho_{ij} + \frac{i}{2}(e^{i(\vec{k}\cdot\vec{z}-\omega t)} + e^{-i(\vec{k}\cdot\vec{z}-\omega t)})(\Omega_{ik}\rho_{kj} - \Omega_{jk}\rho_{ik}) \quad (1)$$

where $\delta_{ij} \equiv \omega_{ij} - i\Gamma_{ij}$; $\Omega_{mn} \equiv \frac{\vec{\mu}_{mn}\cdot\vec{E}}{\hbar}$ is the Rabi frequency; $\vec{\mu}_{mn}$ is the transition moment for the $m \rightarrow n$ transition; and $\vec{E}$, $\vec{k}$, and ω are the electric field, wave vector, and frequency of the excitation pulse, respectively. It neglects Kubo type relaxation, spectral diffusion, and coherence transfer effects. If i and k or j and k are identical, the equation would describe the transition of an initial population to a coherence. The feeding coherences, ρ_{kj} and ρ_{ik}, can oscillate at their free induction decay (FID) frequency or at the excitation field frequency that drives them. For the FID case, we assume $\rho_{kj} = \tilde{\rho}_{kj} e^{i(\omega_{kj}-i\Gamma_{kj})t}$ and $\rho_{ik} = \tilde{\rho}_{ik} e^{i(\omega_{ik}-i\Gamma_{ik})t}$ where the spatial dependence of the phase has been incorporated into the amplitude, $\tilde{\rho}_{mn}$. In order to create a closed form functionality for the transition, we assume a Heaviside excitation pulse that turns on at $t = 0$ and remains constant. The solution is given by

Published: June 6, 2019

DOI: 10.1021/acs.jpclett.9b01280
J. Phys. Chem. Lett. 2019, 10, 2767−2774

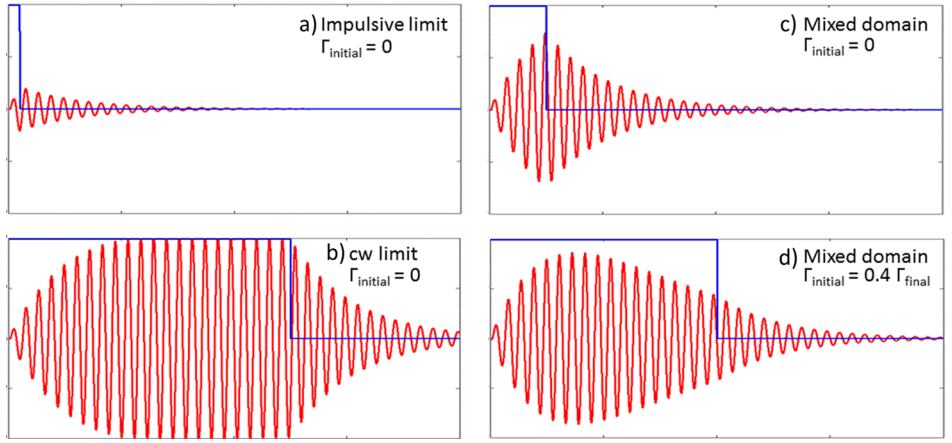

Figure 1. Simulation of coherence transients for different ratios of the dephasing rate to the excitation pulse width. Panels a–c assume an initial static population, while d assumes a dephasing coherence.

$$\rho_{ij} = \rho_{ij}^{0} e^{-i\delta_{ij}t} + \frac{1}{2}\left(\begin{array}{l} \Omega_{ik}\tilde{\rho}_{kj}\left(\dfrac{e^{-i(\delta_{kj}+\omega)t} - e^{-i\delta_{ij}t}}{(\omega_{ik} - \omega - i(\Gamma_{ij} - \Gamma_{kj}))} + \dfrac{e^{-i(\delta_{kj}-\omega)t} - e^{-i\delta_{ij}t}}{(\omega_{ik} + \omega - i(\Gamma_{ij} - \Gamma_{kj}))} \right) \\ - \Omega_{jk}\tilde{\rho}_{ik}\left(\dfrac{e^{-i(\delta_{ik}+\omega)t} - e^{-i\delta_{ij}t}}{(\omega_{kj} - \omega - i(\Gamma_{ij} - \Gamma_{ik}))} + \dfrac{e^{-i(\delta_{ik}-\omega)t} - e^{-i\delta_{ij}t}}{(\omega_{kj} + \omega - i(\Gamma_{ij} - \Gamma_{ik}))} \right) \end{array} \right) \quad (2)$$

Its derivation appears in the Supporting Information. Here, ρ_{ij}^{0} is the initial amplitude of the ij coherence that undergoes FID. The next set of terms describe absorptive and stimulated emission transitions involving $\rho_{kj} \rightarrow \rho_{ij}$ ket-side transitions, respectively. There are two terms in each that control the transient response from the decay of the feeding coherence and the creation of the ρ_{ij} coherence. If the feeding coherence is itself driven and has reached steady state, the second term will describe the initial transient response and the first term will describe the steady state. Note in particular that the frequency of the coherence is changing during the excitation when the feeding coherence is driven off-resonance. The last set of terms describe absorptive and stimulated emission transitions involving $\rho_{ik} \rightarrow \rho_{ij}$ bra-side transitions and the steady-state and transient effects.

If we assume the first term is resonant and ignore the other terms, this equation simplifies to

$$\rho_{ij} = \rho_{ij}^{0} e^{-i\delta_{ij}t} + \frac{i\Omega_{ik}(e^{-\Gamma_{kj}t} - e^{-\Gamma_{ij}t})}{2(\Gamma_{ij} - \Gamma_{kj})}\tilde{\rho}_{kj} e^{-i\omega_{ij}t} \quad (3)$$

There are two experimental limits that are relevant for this expression. Time domain vibrational spectroscopies measure the phase oscillations in the FID of the first term that are then Fourier transformed into spectra. Frequency domain vibrational spectroscopies measure the resonance enhancements described by the second term in the steady state. When the pulse widths are comparable to the dephasing time, the measurement is in the mixed domain where both FID and driven frequencies are important.[18]

Figure 1 shows example transients of eq 2 when the ρ_{kj} feeding coherence is driven and detuned from resonance by $\delta\omega$ and the excitation pulse is constant for a finite time, Δt. Panels a–c of Figure 1 assume the system is initially in the ground state. The transients are representative of excitation pulses (a) in the impulsive limit of time domain CMDS ($1/\Delta t \ll \Gamma_{ij}$), (b) that have reached the steady-state limit of frequency domain CMDS ($1/\Delta t \gg \Gamma_{ij}$), and (c) in the mixed domain ($1/\Delta t \approx \Gamma_{ij}$) where the cw or impulsive approximations are inadequate.[18] In each case,

$$\frac{\rho_{ij}}{\rho_{kj}} = \frac{\Omega_{ij}}{2\Gamma_{ij}} e^{-i\omega_{ij}t}(e^{-i(\pm\delta\omega - i\Gamma_{ij})t} - e^{-i\Gamma_{ij}t})$$

during the excitation pulse and $\rho_{ij}(t) = \rho_{ij}(t = \Delta t)e^{-(i\omega_{ij} - \Gamma_{ij})t}$ after Δt. The ρ_{ij} coherence will rise during the excitation pulse, and its frequency will change as the transient dies away until it matches the excitation frequency and the coherence reaches the steady state. At the end of the excitation pulse, the coherence amplitude ratio is $\frac{\rho_{ij}}{\rho_{kj}} = \frac{\Omega_{ik}}{2\Gamma_{ij}}(1 - e^{-\Gamma_{ij}\Delta t})$, where $\Omega_{ik}/2\Gamma_{ij}$ is the steady-state amplitude. After Δt, the coherence decays exponentially at the ω_{ij} frequency. If the initial ρ_{kj} coherence is undergoing FID, the ρ_{ij} will not reach a steady state and will disappear as the initial ρ_{kj} population decays. Figure 1d represents this case where the pulse width is too long compared with the relaxation times.

Relationships between a Coherence and the Output Signal. It is also important to understand the factors controlling the output signal in the different nonlinear vibrational methods. The output nonlinear polarization created by a coherence launches the output electromagnetic field. The output polarization depends on the coherence amplitude, transition moment, sample concentration, and path length. Neglecting refractive index and local field effects, the output electromagnetic field is related to the nonlinear polarization by

$$\frac{\partial E_{\text{out}}^{0}}{\partial z} + \frac{1}{c}\frac{\partial E_{\text{out}}^{0}}{\partial t} = \frac{2\pi i\omega_{\text{out}}}{c} P_{\text{NL}}^{0} e^{i(\vec{k}_{\text{NL}} - \vec{k}_{\text{out}})l} \quad (4)$$

Here, $\vec{k}_{\text{NL}}$ and $\vec{k}_{\text{out}}$ are the nonlinear polarization and output field wave vectors. If the output field is distinguishable from

DOI: 10.1021/acs.jpclett.9b01280
J. Phys. Chem. Lett. 2019, 10, 2767–2774

the excitation fields and is phase-matched to the nonlinear polarization, the integral of this equation becomes

$$E_{out} = \frac{4\pi\omega_{out}\mu_{out}NL}{c}\tilde{\rho}_{out} \quad (5)$$

where N is the concentration and L is the path length. In typical nonlinear experiments, the highest signal intensities occur when the peak excitation intensities are fixed just below the damage threshold. Because $I_{in} = \frac{c}{8\pi}E_{in}^2$, we can express the corresponding E_{out}/E_{in} ratio as

$$\frac{E_{out}}{E_{in}} = \omega_{out}\mu_{out}NL\sqrt{\frac{\pi}{2cI_{in}}}\tilde{\rho}_{out} \quad (6)$$

Nonlinear infrared vibrational spectroscopy involves absorption transitions induced by one or more excitation beams. In these cases, absorption of the excitation and output beams determine the optimal path length. We approximate this case by postulating that the excitation beam experiencing the greatest absorption defines the path length. This approximation neglects other effects of absorption. Experimentally, the path length is typically determined by the need for an absorbance less than one. Assuming the excitation intensity decrease is $e^{-\alpha L} = e^{-1}$, the effective path length will be $L_{effective} = 1/\alpha$ and the E_{out}/E_{in} ratio will be lowered by $\sim 1/\alpha L$. Because the absorption coefficient itself is related to the same factors as the four-wave mixing signal

$$\alpha = \frac{4\pi\omega_{in}N\mu_{in}^2}{\hbar c\Gamma_{in}} \quad (7)$$

we can write

$$\frac{E_{out}}{E_{in}} = \frac{\hbar\omega_{out}\mu_{out}\Gamma_{in}}{4\omega_{in}\mu_{in}^2}\sqrt{\frac{c}{2\pi I_{in}}}\tilde{\rho}_{out} \quad (8)$$

Alternatively, this expression can also be written in terms of the Rabi frequency created by I_{in}.

$$\frac{E_{out}}{E_{in}} = \frac{\omega_{out}\mu_{out}\Gamma_{in}}{2\omega_{in}\mu_{in}\Omega_{in}}\tilde{\rho}_{out} \quad (9)$$

Note that the ratio does not depend on concentration or path length. Because homodyne detection measures the output intensity, the output signal will scale as the square of this ratio. Heterodyne detection overlaps a local oscillator field with the output field and measures the temporal beating between the two fields:

$$\frac{|E_{out} + E_{LO}|^2}{|E_{LO}|^2} - 1 \approx \frac{2E_{out}}{E_{LO}} \quad (10)$$

if the local oscillator field is substantially higher than the output field. The local oscillator can have either the same intensity as the excitation pulses or an attenuated intensity in order to increase the ratio.

Nonlinear Infrared Vibrational Spectroscopy. Four-wave mixing (FWM) involves three successive interactions occurring within the coherence dephasing times. We first apply this approach to the evolution of coherences in a typical vibrational pathway, $gg \xrightarrow{-1} gv \xrightarrow{2} v'v \xrightarrow{3} v'g$. Because this Viewpoint is developing a simple understanding of how the experimental methodology defines the relative amplitudes of successive coherences, we analyze only this single pathway and assume the perturbative limit where the ground-state population is large compared with the coherences. A full treatment requires calculation of all relevant pathways and the inclusion of excited populations. Here, g, v and v', and e correspond to the ground, vibrational, and electronic states. This pathway occurs in the time domain methods of 2D-IR, SPE, TA, and TG as well as the frequency domain TRIVE spectroscopy.[19] The first interaction creates a coherence from the ground-state population; the second interaction creates a zero quantum coherence between two vibrational states (if v' and v are the same, it is a population), and the last interaction creates the output coherence. The output coherence launches an electromagnetic wave in the direction defined by phase matching, $\vec{k}_4 = -\vec{k}_1 + \vec{k}_2 + \vec{k}_3$. Figure 2 shows example simulations of the coherences in this pathway using Δt = 1 ps or 35 fs rectangular excitation pulses and time delays between pulses of 900 fs. These values are representative of mixed frequency/time domain[8] or time domain CMDS.[20] Our estimates assume the excitation intensity is limited to 10^{10} watts/cm^2 regardless of Δt, because any higher intensity can damage samples. They also assume a transition moment and dephasing rate ($\mu \approx 0.3$ D and $\Gamma \approx 4 \times 10^{13}$ s^{-1}) characteristic of a typical strong carbonyl mode excitation.[21,22] The actual frequencies and amplitudes of each coherence cannot be visualized on a simple graph, so the frequencies and amplitudes in the figure are chosen only for representing the coherences. The actual amplitudes are listed in Table 1. They are normalized to ρ_{gg}^0=1.

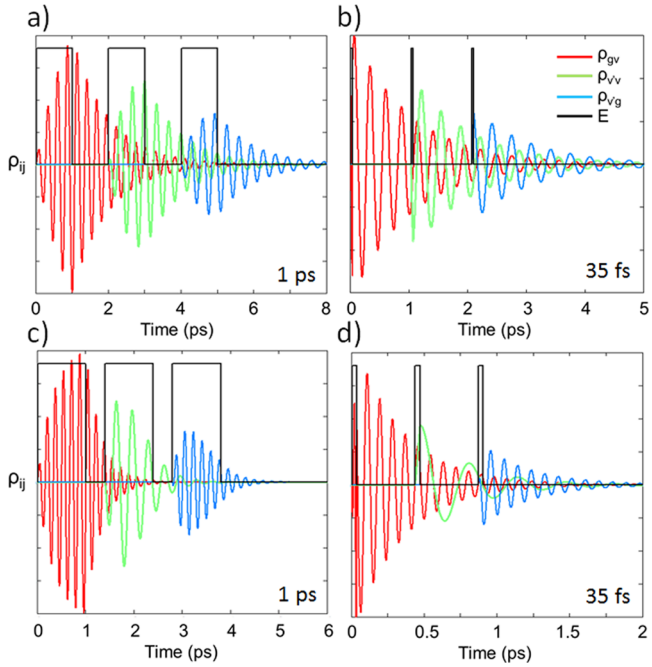

Figure 2. Temporal evolution of the carbonyl coherences created by (a) 1 ps pulses and (b) 35 fs pulses and fingerprint mode coherences created by (c) 1 ps pulses and (d) 35 fs pulses (bottom). The delay time is 900 fs. The delay times were 0.40 and 0.90 ps for the carbonyl and fingerprint mode simulations, respectively. The coherence frequencies and amplitudes are arbitrary and chosen only for visualization. Their actual values appear in Table 1.

Table 1 summarizes the values of each variable and the three carbonyl coherence amplitudes shown in Figure 2 relative to the ground state population. There are three important factors that control the relative amplitude of the three coherences: (1)

DOI: 10.1021/acs.jpclett.9b01280
J. Phys. Chem. Lett. 2019, 10, 2767−2774

Table 1. Summary of the Experimental and Molecular Parameters for Typical Carbonyl and Fingerprint Vibrational Modes and Excitation Pulse Widths and Their Effects on the Amplitude of the Three Coherences or Populations[a]

	$\rho_{initial} \rightarrow \rho_{final}$ Coherence Time Evolution			
I_{excit}	10^{10} watts/cm^2			
Δt	1 ps		35 fs	
mode	carbonyl	fingerprint	carbonyl	fingerprint
delay	400 fs	1 ps	400 fs	1 ps
Γ	3×10^{12} s^{-1}	10^{12} s^{-1}	3×10^{12} s^{-1}	10^{12} s^{-1}
μ	0.3 D	0.01 D	0.3 D	0.01 D
Ω	2.6×10^{12} s^{-1}	8.7×10^{10} s^{-1}	4.2×10^{11} s^{-1}	8.7×10^{10} s^{-1}
$\Omega/2\Gamma$	0.43	0.044	0.43	0.044
$1 - e^{-\Gamma\Delta t}$	0.95	0.63	0.10	0.034
$\rho_{final}/\rho_{initial}$	0.41	0.028	0.043	1.4×10^{-3}
Fully Coherent Pathway Maximum Coherence Amplitudes and Output Signals: 2D-IR, Stimulated Photon Echo, TRIVE				
ρ_{gv}	0.41	0.028	0.041	1.4×10^{-3}
$\rho_{v'v}$	0.020	1.6×10^{-4}	5.2×10^{-4}	7.3×10^{-7}
$\rho_{v'g}$	3.8×10^{-4}	9.5×10^{-7}	6.4×10^{-6}	4.0×10^{-10}
E_{out}/E_{in}	3.3×10^{-4}	1.3×10^{-5}	2.3×10^{-5}	2.7×10^{-8}
$2E_{out}/E_{LO}$	0.068	2.7×10^{-3}	4.8×10^{-3}	5.4×10^{-6}
Partially Coherent Population Pathway Maximum Coherence/Population Amplitudes and Output Signals: Pump−Probe, 2D-IR, Photon Echo				
ρ_{gv}	0.41	0.028	0.043	1.4×10^{-3}
ρ_{vv}	0.078	4.4×10^{-4}	1.8×10^{-3}	2.2×10^{-6}
ρ_{vg}	8.1×10^{-3}	7.0×10^{-6}	3.9×10^{-5}	1.2×10^{-9}
E_{out}/E_{in}	9.3×10^{-3}	3.1×10^{-5}	2.2×10^{-4}	7.9×10^{-8}
$2E_{out}/E_{LO}$	1.9	0.02	0.045	1.6×10^{-5}

[a]The ratios of the output/input field amplitudes or the output/local oscillator field amplitudes characterize homodyne or heterodyne detection methods.

The peak excitation intensity and the transition moment determine the Rabi frequency, and the $\Omega/2\Gamma$ ratio determines the loss of amplitude between the initial and subsequent coherences. (2) The $1 - e^{-\Gamma\Delta t}$ factor determines the fraction of the steady-state coherence amplitude created from a static population. (3) The initial and subsequent coherence dephasing rates relative to the pulse width determine whether the peak of the coherence occurs at the beginning, middle, or end of the excitation pulse. For example, the ρ_{gv} coherence amplitude is 0.41 for the 1 ps pulse as a result of the Rabi/dephasing rate ratio while the 0.043 amplitude for the 35 fs pulse results from both the Rabi/dephasing rate ratio and a smaller fraction of the steady-state coherence amplitude. The $\rho_{v'v}$ coherence amplitude is 20× and 80× lower than the ρ_{gv} coherence for the 1 ps and 35 fs pulses, respectively, because of the additional effects from the high coherence dephasing rate of the previous ρ_{gv} coherence. These effects are clearly seen in Figure 2.

The table also compares the changes in the maximum coherence amplitudes for a vibrational mode in the fingerprint region of the infrared (typically $\mu \approx 0.01$ D and $\Gamma \approx 10^{12}$ s^{-1}). The initial fingerprint mode coherence amplitudes are an order of magnitude lower than the carbonyl mode coherences because the transition moment is smaller and the lower dephasing rate makes the fraction of the steady-state value smaller. The subsequent coherences are lowered further by the dephasing of the previous coherences, although those effects are smaller because the fingerprint mode dephasing rate is slower and the coherences reach their maximum intensity at the end of the excitation pulses (Figure 2c,d).

The output field includes the emission during the driven process while the excitation pulses are present and the FID after the excitation pulses. It is clear from Figure 2 that the driven component of the output signal is the larger contribution to the signal (10× larger) for the 1 ps experiment while the FID component is the larger contribution (100× larger) for the 35 fs experiment. Table 1 summarizes the intensity ratios for homodyne detection, $(E_{out}/E_{in})^2$, and heterodyne detection, $2E_{out}/E_{LO}$, using eqs 9 and 10, respectively. The $\tilde{\rho}_{out}$ parameter in these equations includes integrating over both the driven and FID contributions. The table values assume a local oscillator intensity of 2×10^{-4} of an excitation pulse intensity, a typical choice for achieving low detection limits.[23−25] This factor includes both the attenuation and the broad frequency bandwidth of the local oscillator relative to the spectral width of the vibrational transition.

Comparison between the intensity ratios of the 1 ps and 35 fs experiments shows the carbonyl signal levels from the 1 ps experiment are 3 orders of magnitude larger than the 35 fs experiment and 5 orders of magnitude larger for the fingerprint mode. Further, the signal levels for the 1 ps fingerprint mode are comparable to those from the 35 fs carbonyl mode. These differences relate directly to the extensive use of 2D-IR to probe carbonyl and other modes with very large transition moments, particularly for experiments where these modes are used as molecular labels to probe dynamics at specific spots in a molecule.[26] 2D-IR has not been used for the spectroscopy of fingerprint modes because of these differences in signal levels. The exception is relaxation-assisted 2D-IR.[24] Here, a pump excitation excites carbonyl or other strong vibrational transitions. The carbonyl mode then undergoes population relaxation to other modes which can then be observed with the probe pulse. Direct excitation and detection has not yet been successful for typical fingerprint modes.[23]

It is more common to use partially coherent methods that create a population, ρ_{vv}, after the first two interactions.[23] These methods include pump−probe,[11] 2D-IR,[24] and photon echo.[27] Table 1 summarizes the coherence and population amplitudes

DOI: 10.1021/acs.jpclett.9b01280
J. Phys. Chem. Lett. 2019, 10, 2767−2774

Table 2. Summary of Coherence Amplitudes for Different Raman-based CMDS Methods and the Values Required to Calculate the Amplitudes and Conversion Efficiencies[a]

$\chi^{(3)}_{\mathrm{CARS}}$	5.75×10^{-15} cm^3/erg
$\chi^{(3)}_{\mathrm{DOVE}}$	3.1×10^{-14} cm^3/erg
N	1.97×10^{22} cm^{-3}
$\omega_{\mathrm{visible}}$	18 797 cm^{-1}
I_{excit}	10^{10} watts/cm^2

DOVE		TRSF		CARS	
ω_{vg}	918 cm^{-1}	ω_{vg}	918 cm^{-1}	ω_{vg}	918 cm^{-1}
$\omega_{v'g}$	2253 cm^{-1}	$\omega_{v'g}$	2253 cm^{-1}	$\omega_{v'g}$	–
$\omega_{(v+v'),g}$	3164 cm^{-1}	$\omega_{(v+v'),g}$	3164 cm^{-1}	$\omega_{(v+v'),g}$	–
ω_{eg}	77000 cm^{-1}	ω_{eg}	77000 cm^{-1}	ω_{eg}	77000 cm^{-1}
μ_{gv}	0.027 D	μ_{gv}	0.027 D	μ_{gv}	–
$\mu_{gv'}$	–	$\mu_{v,v+v'}$	0.025 D	$\mu_{gv'}$	–
$\mu_{g,(v+v')}$	0.0064 D		0.0064 D	$\mu_{g,(v+v')}$	–
$\mu_{(v+v'),(e+\ v')}$	1.14 D	$\mu_{(v+v'),(e+\ v')}$	1.14 D	μ_{ge}, μ_{ev}	1.14 D
Γ_{vg}	2.72 cm^{-1}	Γ_{vg}	2.72 cm^{-1}	Γ_{vg}	2.72 cm^{-1}
$\Gamma_{v'g}$	2.85 cm^{-1}	$\Gamma_{v'g}$	2.85 cm^{-1}	$\Gamma_{v'g}$	–
$\Gamma_{(v+v'),\ g}$	4.39 cm^{-1}	$\Gamma_{(v+v'),\ g}$	4.39 cm^{-1}	$\Gamma_{(v+v'),\ g}$	–
$\Omega_{gv'}$	2.0×10^{11} s^{-1}	$\Omega_{gv'}$	5.4×10^{11} s^{-1}	$\Omega_{gv'}$	–
$\Omega_{g,(v+v')}$	5.8×10^{10} s^{-1}	$\Omega_{g,(v+v')}$	2.4×10^{11} s^{-1}	$\Omega_{g,(v+v')}$	–
$\Omega_{(v+v'),(e+v')}$	9.9×10^{12} s^{-1}	$\Omega_{(v+v'),(e+v')}$	9.9×10^{12} s^{-1}	Ω_{ge}, Ω_{ev}	9.9×10^{12} s^{-1}

DOVE coherence amplitudes			TRSF coherence amplitudes			SRS and CARS coherence amplitudes		
Δt	1000 fs	35 fs	Δt	1000 fs	35 fs	Δt	1000 fs	35 fs
ρ_{gv}	0.079	3.5×10^{-3}	ρ_{vg}	0.079	3.5×10^{-3}	ρ_{eg}	4.5×10^{-4}	4.5×10^{-4}
$\rho_{\mathrm{v+v',v}}$	7.1×10^{-4}	2.2×10^{-6}	$\rho_{\mathrm{v+v',g}}$	3.3×10^{-3}	8.5×10^{-6}	ρ_{vg}	1.6×10^{-3}	7.5×10^{-5}
$\rho_{\mathrm{e+v,v}}$	1.3×10^{-7}	4.9×10^{-10}	$\rho_{\mathrm{e+v,g}}$	8.1×10^{-7}	2.6×10^{-9}	ρ_{eg}	4.7×10^{-7}	2.1×10^{-8}
$E_{\mathrm{out}}/E_{\mathrm{in}}$	4.0×10^{-5}	2.2×10^{-7}	$E_{\mathrm{out}}/E_{\mathrm{in}}$	2.8×10^{-4}	1.2×10^{-6}	$E_{\mathrm{out}}/E_{\mathrm{in}}$[b]	5.3×10^{-2}	5.1×10^{-3}

[a] The top of the table summarizes the experimental values used for calculating the coherence amplitudes for each of the different pathways involving a Raman transition.[9,11] The energy of the electronic state corresponds to the lowest excited electronic state of acetonitrile. The transition moment of the electronic state is chosen to correspond to the measured third-order susceptibility. The lower part of the table summarizes the amplitudes of the three coherences involved in each four-wave mixing process for the 1 ps and 35 fs pulses. The last entries summarize the ratio of the output pulse intensity to an input pulse intensity (10^{10} watts/cm^2). Details of the calculations appear in the Supporting Information. [b] Values for a 1 mm path length.

when the first two pulses are temporally overlapped. The amplitude of the individual coherences increases as a result of the temporal overlap and allows an increase in the typical local oscillator field to 0.01 of the original excitation beam.[23] The increase in the coherence amplitude is less than an order of magnitude; therefore, the signals from the fingerprint modes are still too weak to make their spectroscopy feasible.

Nonlinear Vibrational Spectroscopy Involving Raman Transitions. In addition to the infrared CMDS methods that excite coherences directly, there are also many nonlinear vibrational methodologies that involve a Raman transition.[11−14,28,29] Historically, these CMDS methods evolved from coherent Raman methods that focused on obtaining vibrational spectra, not dynamics. These methods were based in the frequency domain and were able to measure vibrational modes over the entire fingerprint region.[30−34] The inclusion of a Raman excitation in fully coherent CMDS pathways creates output coherences in the visible and ultraviolet regions where single-photon detection methods are possible. These pathways are particularly useful because the output signal can be spectrally resolved from the excitation frequencies so single-photon detection becomes possible.[35] Because the pathways are fully coherent, they are immune to population relaxation. The coupled quantum states create multidimensional molecular fingerprints.[35] Complications from relaxation effects are avoided because relaxation collapses the entangled Schrödinger cat states and destroys the emission. The coupling between quantum states manifests through the requirement that the pathways involve an overtone and combination band state in an infrared or Raman transition. These methods can also provide a very powerful approach for performing pump−probe experiments on complex samples where spectral congestion prevents resolution of individual spectral features. If the probe is a fully coherent pathway, it can provide a multidimensional fingerprint of specific molecules within the complex sample that can identify the population dynamics that follow the pump. This pump−fully coherent probe is already the basis for FSRS.[17,36]

We consider four methodologies that are important in vibrational CMDS: doubly vibrationally enhanced (DOVE) spectroscopy,[9−11] triply resonant sum frequency (TRSF) spectroscopy,[12−14] stimulated Raman spectroscopy (SRS),[17,31,36] and coherent anti-Stokes Raman spectroscopy (CARS).[15] Example pathways for these four methods are

$$gg \xrightarrow{-2} gv' \xrightarrow{1} (v' + v),\ v' \xrightarrow{3} (e + v'),\ v';$$

$$gg \xrightarrow{1} vg \xrightarrow{2} (v' + v),\ g \xrightarrow{3} (e + v'),\ g;$$

$gg \xrightarrow{-1} ge \xrightarrow{2} gv \xrightarrow{3} ev$; and $gg \xrightarrow{1} eg \xrightarrow{-2} vg \xrightarrow{3} eg$, respectively. Here, the numbers denote the excitation frequencies and phase matching, not the time ordering. In the DOVE pathway, the first two interactions involve infrared excitation of a fundamental (v') and a combination band (v+v').[11] The last

interaction involves an amplitude level Raman transition. In the TRSF pathway, the first two interactions successively excite two fundamental modes to create an overtone or combination band (v+v') and a Raman transition to an electronic state that is coupled to both modes.[12−14] In the SRS pathway, a Raman transition excites a vibrational coherence and the final output field heterodynes with field 2 to increase its intensity. In the CARS pathway, there are two amplitude level interactions that both involve a vibrational mode (v).[15] In each case, the output intensity depends only on the driven Raman process during the excitation pulses because the electronic dephasing is so fast that FID is negligible. Modeling for the Raman transition differs from that used for the infrared transitions because the rapid dephasing of the virtual or real electronic state requires the temporal overlap of the Raman excitation pulses. Because FID is negligible, the driven process defines the Raman coherence transition. The implementation of the modeling for the Raman transitions is described in the Supporting Information.

Detailed measurements of the required variables are available for both DOVE and CARS experiments of acetonitrile C−C and C≡N stretch modes that correspond to v and v'.[9,11] The v, v', and $(e+v')$,v' states of acetonitrile are summarized in Table 2 along with the measured transition dipoles and dephasing rates for the infrared transitions. The table also includes the measured third-order susceptibility for a CARS and a DOVE feature.[9] The third-order susceptibilities for each process are given by $\chi^{(3)}_{CARS} = \frac{NF\mu_{eg}^2\mu_{ev}^2}{4D\hbar^3\Delta^1_{eg}\Delta^{1-2}_{vg}\Delta^{1-2+3}_{eg}}\rho_{gg}$ and $\chi^{(3)}_{DOVE} = \frac{NF\mu_{gv'}\mu_{g,(v+v')}\mu_{(v+v'),(e+v')}\mu_{(e+v'),v'}}{4D\hbar^3\Delta^{-2}_{gv'}\Delta^{1-2}_{(v+v'),v'}\Delta^{1-2+3}_{(e+v'),v'}}\rho_{gg}$. Here, D is the degeneracy factor of 6 in the Maker−Terhune convention for a three-color pathway,[37] N the concentration, F a local field correction, and $\Delta^{i-j}_{nm} \equiv \omega_{nm} - \omega_i + \omega_j - i\Gamma_{nm}$ the detuning factor. These equations assume that a single electronic state is responsible for the electronic transition. The acetonitrile experiment lacked an electronic resonance, so a correct treatment requires a summation over the frequencies and transition moments of all coupled virtual electronic states. Here, we assume that a single electronic detuning factor and transition moment is representative of the virtual states, that the detuning is large compared with the dephasing rate, and that all electronic transition moments are the same.

Because the CARS and DOVE third-order susceptibility measurements used the same vibrational states, it is possible to approximate the μ^2_{eg}/Δ_{eg} ratio that determines the coherence steady state for the $\rho_{(v+v'),v'} \rightarrow \rho_{(e+v'),v'}$ and $\rho_{(e+v'),v'} \rightarrow \rho_{v'v'}$ transitions. Note that knowledge of the third-order susceptibilities does not allow calculation of μ_{eg} and Δ_{eg} separately. Instead, we estimate the detuning is at least ∼77 000 cm^{-1} from the onset of the acetonitrile absorption bands. It is now possible to obtain the corresponding value for μ_{eg} from the μ^2_{eg}/Δ_{eg} ratio. This estimate is conservative because larger detuning values would increase the transition moment estimate. Finally, the high dephasing rate of the virtual electronic state will eliminate FID and the Raman process will correspond to the steady state.

Table 2 summarizes the values required to implement this strategy as well as the values for the three coherences involved in the CARS and DOVE pathways and the E_{out}/E_{in} conversion efficiency determined by eq 6. These values can be directly compared with those in Table 1. Note that the very high conversion efficiency for CARS results because the path length is not determined by infrared absorption of vibrational modes, so a longer path length is possible. The values in Table 2 used a 1 mm path length that is typical of a CARS experiment.

The large detuning involved in the nonresonant Raman transitions of DOVE, TRSF, SRS, and CARS pathways makes an electronic coherence 5 orders of magnitude lower than the previous coherence and 2 orders of magnitude lower than the coherences created by infrared transitions. Despite the lower conversion efficiency, the output coherences for a DOVE, TRSF, SRS, or CARS process using 1 ps or 35 fs pulses are comparable to those of the fingerprint mode in Table 1 and the E_{out}/E_{in} conversion efficiency is actually larger. The large detuning factor associated with nonresonant Raman transitions is offset by the larger electronic transition moments and the resultant Rabi frequencies. It is noteworthy that the second coherence, $\tilde{\rho}_{vg}$, for the SRS and CARS process with a 1 ps pulse is actually larger than the $\tilde{\rho}_{eg}$ coherence that preceded it. This result occurs because the first and second excitation pulses are temporally overlapped. The $\tilde{\rho}_{eg}$ amplitude has reached steady state because $\Omega_{eg}/\Gamma_{eg} \ll 1$ while the $\tilde{\rho}_{vg}$ amplitude can grow rapidly because $\Omega_{vg}/\Gamma_{vg} > 1$. Under these conditions, the first coherence quickly reaches a low steady-state amplitude that continuously feeds the second coherence and allows its buildup. It is also interesting that the TRSF output coherence and conversion efficiency is significantly larger than that for the DOVE pathway. The higher conversion efficiency is observed experimentally. This increased signal results because the infrared transitions are allowed for the TRSF coherence, whereas the DOVE pathway involves a combination band or overtone transition.

Experimental Considerations. There are other experimental factors that enter into the comparisons between different approaches. The delay time and duty cycle are very important factors in defining the output field, not only for maximizing coherence amplitudes and total signal but also for controlling the effects of nonresonant background interference.[15] The nonresonant background poses a fundamental limit to measuring weak vibrational transitions. It arises because the large transition moment of electronic transitions makes larger electronic nonlinearities than vibrational nonlinearities.[38] The first vibrational CMDS experiments used neat acetonitrile for a doubly vibrationally enhanced (DOVE) CMDS experiment that excited a weak combination band and a fundamental mode. The third interaction was nonresonant. The experiment determined a third-order nonlinear susceptibility of $\chi^{(3)} = 3.1 \times 10^{-14}$ cm^3/erg for the DOVE CMDS pathway and 1.7×10^{-15} cm^3/erg for the nonresonant $\chi^{(3)}$.[9] They differed only by an order of magnitude. Discrimination against the nonresonant background is usually based on inserting a delay time between two excitation pulses.[39] The nonresonant background signal dephases almost instantaneously while the vibrational coherence dephases slowly. In practice, excitation pulses are not rectangular and always have some temporal overlap. Optimizing the discrimination involves controlling the temporal overlap between the excitation pulses by adjusting the delay times or the excitation pulse widths. Shorter pulses provide greater discrimination but lower coherence amplitudes. The optimum trade-off typically occurs when the dephasing time and pulse widths are similar.

If the nonresonant signal is not important, the detection limit for homodyne detection depends on the efficiency of photon detection. For heterodyne detection, the detection

DOI: 10.1021/acs.jpclett.9b01280
J. Phys. Chem. Lett. 2019, 10, 2767−2774

limit is determined by the fluctuations in the local oscillator, typically $|\Delta E_{LO}/E_{LO}|^2 \approx 0.02$.[23] Because fully coherent CMDS methods involving Raman transitions often have output frequencies that are spectrally distinct from excitation pulse scatter, the detection limits can be extended to much less than one photon/pulse. In this case, the detection limit depends on the pulse repetition rate. Higher repetition rates increase the duty cycle so the detection limits scale as the square root of the rate. Higher repetition rates also decrease the pulse energy. To maintain the same high peak intensity required for efficient FWM, an experiment would focus the excitation beams more tightly. This strategy is therefore well-adapted for high-resolution microscopy. In this high repetition rate regime, homodyne detection may become the preferred detection method because of its capability for single-photon detection.

The duty cycle is a very important parameter in defining whether single-molecule vibrational spectroscopy is possible. In single-molecule fluorescence detection, the excitation is continuous, and the intensities are ~10 kW/cm^2. For a 1 D electronic transition, the Rabi frequency is 1.4×10^9 s^{-1}. The relaxation rate for a fluorescence transition is typically 10^8 s^{-1} so the transition is saturated and the output coherence $\rho_{eg} \geq 0.5$. The typical output coherences for the nonlinear vibrational experiments create output coherences that are at least 2 orders of magnitude smaller, depending on the transition moment and pulse width, and the duty cycles are typically 10^{-9}. It is clear that the low duty cycle and output coherence will prevent single-molecule detection with current technology. Single-molecule vibrational spectroscopy will require nearly continuous excitation and submicrometer spot sizes to reach the intensities required for a feasible single-molecule CMDS experiment. Even here, there are important questions about nonresonant processes and the loss of the directional emission that results from cooperative emission. Nevertheless, it is clear that the ability to control the pulse width and the repetition rate of the excitation pulses will provide the flexibility to optimize experiments, particularly experiments involving vibrational spectra.

Conclusions. Partially and fully coherent methodologies form a complementary and closely related family of spectroscopic tools. Methods like 2D-IR are a partially coherent methodology where the initial and final coherences are cat states that are immune to population dynamics. They are separated by a delay time where the cat state collapses into populations that are probed by the last coherence. It is able to measure ultrafast dynamics with a spectral clarity that is superior to pump–probe methods. Fully coherent methods use the coupled states to provide multidimensional fingerprints that are immune to population relaxation dynamics and cover wide spectral ranges and many different modes. They can also be used as a multidimensional probe of population relaxation dynamics that follows a pump as FSRS already demonstrates. Currently, experimental systems are constrained to one of these methodologies. This Viewpoint has identified the importance of pulse width and duty cycle as the key factors that control the capabilities of the different CMDS methodologies. If the technology evolves to control these factors, the capabilities will be greatly expanded. Just as the technology of NMR evolved to implement the entire family of NMR methods, so also must the technology of CMDS evolve from its focus on measuring dynamics to a focus on making CMDS available to the broader scientific community. The results can be transformative. Spectroscopy is ubiquitous across all fields of science, but it is often hampered by the spectral congestion of complex samples. The spectral selectivity of CMDS allows it to resolve congested spectra and to identify the coupling and interactions between states and the evolution of the states on a wide range of time scales. These are exactly the capabilities required to solve the most difficult problems encountered today. The development of a more versatile CMDS technology can greatly expand the capabilities of all fields of science that use spectroscopic methods.

John C. Wright*

Department of Chemistry, University of Wisconsin—Madison, 1101 University Avenue, Madison, Wisconsin 53706, United States

■ ASSOCIATED CONTENT

Supporting Information

The Supporting Information is available free of charge on the ACS Publications website at DOI: 10.1021/acs.jpclett.9b01280.

A derivation of eq 2, the derivation of the equations used to model the results summarized in Tables 1 and 2, and simulations of spectra resulting from Gaussian or rectangular excitation pulses (PDF)

■ AUTHOR INFORMATION

ORCID

John C. Wright: 0000-0002-6926-1837

Notes

The author declares no competing financial interest.

■ ACKNOWLEDGMENTS

This work was supported by the National Science Foundation under Grant CHE-1709060. The author acknowledges helpful discussions with Martin Zanni, Igor Rubtsov, Nien-Hui Ge, Junrong Zheng, Christopher Cheetham, and Daniel Kohler.

■ REFERENCES

(1) Mukamel, S. *Principles of Nonlinear Optical Spectroscopy*, 1st ed.; Oxford University Press: New York, 1995.

(2) Hamm, P.; Lim, M.; DeGrado, W. F.; Hochstrasser, R. M. The Two Dimensional IR Nonlinear Spectroscopy of a Cyclic Penta-Peptide in Relation to its Three-Dimensional Structure. *Proc. Natl. Acad. Sci. U. S. A.* **1999**, *96*, 2036–2041.

(3) Hamm, P.; Lim, M.; DeGrado, W. F.; Hochstrasser, R. M. Stimulated Photon Echoes from Amide I Vibrations. *J. Phys. Chem. A* **1999**, *103*, 10049–10053.

(4) Hamm, P.; Lim, M.; DeGrado, W. F.; Hochstrasser, R. M. Pump/Probe Self Heterodyned 2D Spectroscopy of Vibrational Transitions in a Small Globular Protein. *J. Chem. Phys.* **2000**, *112*, 1907–1916.

(5) Tokmakoff, A.; Fayer, M. D. Infrared Photon Echo Experiments: Exploring Vibrational Dynamics in Liquids and Glasses. *Acc. Chem. Res.* **1995**, *28*, 437–445.

(6) Laubereau, A.; Kaiser, W. Vibrational Dynamics of Liquids and Solids Investigated by Picosecond Light-Pulses. *Rev. Mod. Phys.* **1978**, *50*, 607–665.

(7) Rentzepis, P. M. Ultrafast Processes. *Science* **1970**, *169*, 239–247.

(8) Meyer, K. A.; Besemann, D. M.; Wright, J. C. Coherent Two Dimensional Spectroscopy with Triply Vibrationally Enhanced Infrared Four Wave Mixing. *Chem. Phys. Lett.* **2003**, *381*, 642–649.

(9) Zhao, W.; Wright, J. C. Measurement of chi(3) for Doubly Vibrationally Enhanced Four Wave Mixing Spectroscopy. *Phys. Rev. Lett.* **1999**, *83*, 1950–1953.

DOI: 10.1021/acs.jpclett.9b01280
J. Phys. Chem. Lett. 2019, 10, 2767–2774

(10) Zhao, W.; Wright, J. C. Spectral Simplification in Vibrational Spectroscopy Using Doubly Resonant Infrared Four Wave Mixing. *J. Am. Chem. Soc.* **1999**, *121*, 10994−10998.
(11) Zhao, W.; Wright, J. C. Doubly Vibrationally Enhanced Four Wave Mixing Spectroscopy: The Optical Analogue to 2D NMR. *Phys. Rev. Lett.* **2000**, *84*, 1411−1414.
(12) Boyle, E. S.; Neff-Mallon, N. A.; Handali, J. D.; Wright, J. C. Resonance IR: a coherent multidimensional analogue of resonance Raman. *J. Phys. Chem. A* **2014**, *118*, 3112−3119.
(13) Boyle, E. S.; Neff-Mallon, N. A.; Wright, J. C. Triply Resonant Sum Frequency Spectroscopy: Combining Advantages of Resonance Raman and 2D-IR. *J. Phys. Chem. A* **2013**, *117*, 12401−12408.
(14) Boyle, E. S.; Pakoulev, A. V.; Wright, J. C. Fully Coherent Triple Sum Frequency Spectroscopy of a Benzene Fermi Resonance. *J. Phys. Chem. A* **2013**, *117*, 5578−5588.
(15) Tolles, W. M.; Nibler, J. W.; McDonald, J. R.; Harvey, A. B. Review of Theory and Applications of Coherent Anti-Stokes Raman Spectroscopy. *Appl. Spectrosc.* **1977**, *31*, 253−271.
(16) Maier, M. Applications of Stimulated Raman Scattering. *Appl. Phys.* **1976**, *11*, 209−231.
(17) Dietze, D. R.; Mathies, R. A. Femtosecond Stimulated Raman Spectroscopy. *ChemPhysChem* **2016**, *17*, 1224−1251.
(18) Kohler, D. D.; Thompson, B. J.; Wright, J. C. Multi-Resonant Coherent Multidimensional Spectroscopy When Dephasing Rivals Pulsewidth: Disentangling Material and Instrument Response. *J. Chem. Phys.* **2017**, *147*, 084202−084219.
(19) Wright, J. C. Multiresonant Coherent Multidimensional Spectroscopy. *Annu. Rev. Phys. Chem.* **2011**, *62*, 209−230.
(20) Hamm, P.; Lim, M.; Hochstrasser, R. M. Structure of the Amide I Band of Peptides Measured by Femtosecond Nonlinear-Infrared Spectroscopy. *J. Phys. Chem. B* **1998**, *102*, 6123−6138.
(21) Mukherjee, P.; Kass, I.; Arkin, I.; Zanni, M. T. Picosecond dynamics of a membrane protein revealed by 2D IR. *Proc. Natl. Acad. Sci. U. S. A.* **2006**, *103*, 3528−3533.
(22) Spexard, M.; Immeln, D.; Thöing, C.; Kottke, T. Infrared spectrum and absorption coefficient of the cofactor flavin in water. *Vib. Spectrosc.* **2011**, *57*, 282−287.
(23) Rock, W.; Li, Y. L.; Pagano, P.; Cheatum, C. M. 2D IR Spectroscopy using Four-Wave Mixing, Pulse Shaping, and IR Upconversion: A Quantitative Comparison. *J. Phys. Chem. A* **2013**, *117*, 6073−6083.
(24) Kurochkin, D. V.; Naraharisetty, S. R. G.; Rubtsov, I. V. A relaxation-assisted 2D IR spectroscopy method. *Proc. Natl. Acad. Sci. U. S. A.* **2007**, *104*, 14209−14214.
(25) Kurochkin, D. V.; Naraharisetty, S. R. G.; Rubtsov, I. V. Dual-frequency 2D IR on interaction of weak and strong IR modes. *J. Phys. Chem. A* **2005**, *109*, 10799−10802.
(26) Ghosh, A.; Ostrander, J. S.; Zanni, M. T. Watching Proteins Wiggle: Mapping Structures with Two-Dimensional Infrared Spectroscopy. *Chem. Rev.* **2017**, *117*, 10726−10759.
(27) Merchant, K. A.; Thompson, D. E.; Fayer, M. D. Two-dimensional time-frequency ultrafast infrared vibrational echo spectroscopy. *Phys. Rev. Lett.* **2001**, *86*, 3899−3902.
(28) Wright, J. C. Applications of the New Family of Coherent Multidimensional Spectroscopies for Analytical Chemistry. *Annu. Rev. Anal. Chem.* **2017**, *10*, 45−70.
(29) Pakoulev, A. V.; Rickard, M. A.; Kornau, K. M.; Mathew, N. A.; Yurs, L. A.; Block, S. B.; Wright, J. C. Mixed Frequency-/Time-Domain Coherent Multidimensional Spectroscopy: Research Tool or Potential Analytical Method? *Acc. Chem. Res.* **2009**, *42*, 1310−1321.
(30) Kaiser, W.; Maier, M.; Giordmaine, J. A. Vibrational Interaction in Mixed Liquids during Stimulated Raman Action. *Appl. Phys. Lett.* **1965**, *6*, 25−26.
(31) Maier, M. Applications of Stimulated Raman-Scattering. *Appl. Phys.* **1976**, *11*, 209−231.
(32) Owyoung, A.; Jones, E. D. Coherent Detection of Raman Modes by Cw Stimulated Raman Gain Spectroscopy. *IEEE J. Quantum Electron.* **1977**, *13*, 912.
(33) Begley, R. F.; Harvey, A. B.; Byer, R. L.; Hudson, B. S. Raman-Spectroscopy with Intense, Coherent, Anti-Stokes Beams. *J. Chem. Phys.* **1974**, *61*, 2466−2467.
(34) Tolles, W. M.; Nibler, J. W.; Mcdonald, J. R.; Harvey, A. B. Review of Theory and Application of Coherent Anti-Stokes Raman-Spectroscopy (Cars). *Appl. Spectrosc.* **1977**, *31*, 253−271.
(35) Wright, J. C. Analytical chemistry, multidimensional spectral signatures, and the future of coherent multidimensional spectroscopy. *Chem. Phys. Lett.* **2016**, *662*, 1−13.
(36) Fang, C.; Frontiera, R. R.; Tran, R.; Mathies, R. A. Mapping GFP structure evolution during proton transfer with femtosecond Raman spectroscopy. *Nature* **2009**, *462*, 200−204.
(37) Maker, P. D.; Terhune, R. W. Study of optical effects due to an induced polarization third order in the electric field. *Phys. Rev.* **1965**, *137*, A801−A818.
(38) Labuda, M. J.; Wright, J. C. Measurement of Vibrationally Resonant Chi3 and the Feasibility of Selective Four Wave Mixing. *Phys. Rev. Lett.* **1997**, *79*, 2446−2450.
(39) Kamga, F. M.; Sceats, M. G. Pulse-Sequenced Coherent Anti-Stokes Raman Scattering Spectroscopy: A Method For Suppression of the Nonresonant Background. *Opt. Lett.* **1980**, *5*, 126−128.

DOI: 10.1021/acs.jpclett.9b01280
J. Phys. Chem. Lett. 2019, 10, 2767−2774